nature astronomy

ARTICLES

https://doi.org/10.1038/s41550-021-01426-9

Check for updates

A sublimated water atmosphere on Ganymede detected from Hubble Space Telescope observations

Lorenz Roth[1]✉, Nickolay Ivchenko[1], G. Randall Gladstone[2], Joachim Saur[3], Denis Grodent[4], Bertrand Bonfond[4], Philippa M. Molyneux[2] and Kurt D. Retherford[2]

Ganymede's atmosphere is produced by charged particle sputtering and sublimation of its icy surface. Previous far-ultraviolet observations of the O I 1,356 Å and O I 1,304 Å oxygen emissions were used to infer sputtered molecular oxygen (O_2) as an atmospheric constituent, but an expected sublimated water (H_2O) component remained undetected. Here we present an analysis of high-sensitivity spectra and spectral images acquired by the Hubble Space Telescope revealing H_2O in Ganymede's atmosphere. The relative intensity of the oxygen emissions requires contributions from the dissociative excitation of water vapour, indicating that H_2O is more abundant than O_2 around the subsolar point. Away from the subsolar region, the emissions are consistent with a pure O_2 atmosphere. Eclipse observations constrain atomic oxygen to be at least two orders of magnitude less abundant than these other species. The higher H_2O/O_2 ratio above the warmer trailing hemisphere compared with the colder leading hemisphere, the spatial concentration in the subsolar region and the estimated abundance of ~10^{15} molecules of H_2O per cm^2 are consistent with sublimation of the icy surface as source.

Through erosion of Ganymede's icy surface by charged particles and solar radiation, a tenuous atmosphere formed consisting of water group molecules and atoms (H_2O, O_2, OH, H and O)[1,2]. Molecular oxygen has long been suspected to be the most abundant constituent globally, as it does not efficiently react with the surface and is gravitationally bound. The lighter products of ice surface erosion, H and H_2, escape quickly and are less abundant[2]. H_2O freezes on contact with the ice surface, which has temperatures between ~80 K and ~150 K (refs. [3,4]), which also limits the lifetime and abundance of H_2O in the atmosphere. Atmospheric modelling efforts suggest a dichotomy in the atmosphere between an H_2O-dominated atmosphere near the subsolar point where the surface is warmest, and an O_2-dominated atmosphere everywhere else[4–7].

The abundance of molecular oxygen and atomic hydrogen have been confirmed observationally in several studies. Atomic hydrogen was detected through measurements of resonantly scattered solar Lyman α emission in an extended corona[8–10]. The first evidence for oxygen was provided by far-ultraviolet (FUV) spectra taken by the Hubble Space Telescope (HST) of oxygen emissions near 1,304 Å and 1,356 Å (ref. [11]). The relative brightness of the emissions from the spin forbidden O I (^5S–^3P) 1,356 Å doublet and the optically allowed O I (^3S–^3P) 1,304 Å triplet was used as a diagnostic of the excitation process. The derived O I 1,356 Å/O I 1,304 Å oxygen emission ratio (denoted r_γ(O I) hereafter) of 1.3 ± 0.3 was interpreted as relating to the global dissociative excitation of O_2 by electrons. The reasoning is that electron-impact excitation processes that involve other possible species in the atmosphere such as O or H_2O produce substantially brighter 1,304 Å emissions (r_γ(O I) < 1)[12–14]. In addition, resonant scattering of solar emissions by atomic oxygen contributes to the O I 1,304 Å brightness but is absent at 1,356 Å (ref. [15]). Electron impact excitation of O_2, in contrast, results in a larger oxygen emission ratio of r_γ(O I) > 2 (ref. [16]). The same diagnostic was used to derive O_2 in the atmospheres of Europa[15,17] and Callisto[18].

The first FUV images of Ganymede revealed that the O I 1,356 Å emissions on the orbital trailing hemisphere of Ganymede are clustered near the magnetic (and planetocentric) poles, similar to the appearance of auroral bands[9]. Further images of the orbital leading and sub-Jovian hemispheres revealed different oxygen emission morphologies, which showed that the regions of brightest O I 1,356 Å emissions are roughly co-located with the open–closed field line boundary of Ganymede's mini-magnetosphere[19]. On the orbital leading hemisphere, which is also the plasma downstream or wake hemisphere, the band-like emissions are close to the equator, as the magnetosphere is stretched due to magnetic stresses[19,20]. The high-latitude emissions observed on the trailing hemisphere, which is also the plasma upstream hemisphere, are consistent with a compressed magnetosphere pushing the open–closed field line boundary further towards the poles[21].

Further observations and analysis of r_γ(O I) on Ganymede's trailing and leading hemispheres showed a consistently higher value (r_γ(O I) ≳ 2) on the leading hemisphere compared with the trailing hemisphere (r_γ(O I) < 2) (refs. [9,22]). The low ratio on the trailing hemisphere was interpreted as being related to a higher mixing ratio of atomic oxygen in the O_2 atmosphere of ≳10% (ref. [22]), similar to interpretations of Europa's oxygen emission ratios[11,15,17]. The absolute observed O I 1,304 Å intensity together with the low oxygen ratio requires a substantial amount of O, putting the O atmosphere in an optically thick range at O I 1,304 Å (ref. [22]).

Studies of the spatial distribution have so far been based almost entirely on the O I 1,356 Å emission (rather than the O I 1,304 Å emission) because the signal-to-noise ratio is considerably higher

[1]Space and Plasma Physics, KTH Royal Institute of Technology, Stockholm, Sweden. [2]Southwest Research Institute, San Antonio, TX, USA. [3]Institut für Geophysik und Meteorologie, Universität zu Köln, Cologne, Germany. [4]Laboratoire de Physique Atmosphérique et Planétaire, STAR Institute, Université de Liége, Liége, Belgium. ✉e-mail: lorenzr@kth.se

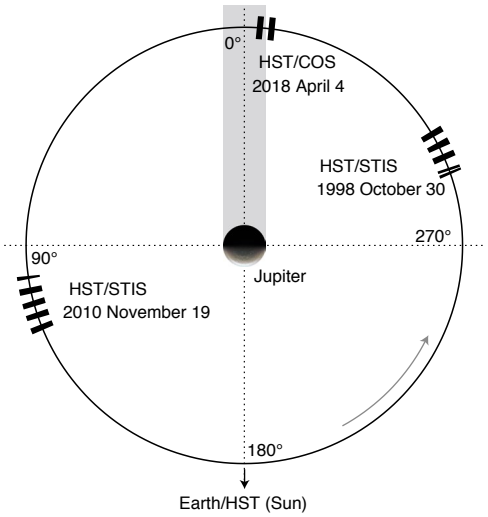

Fig. 1 | Ganymede's orbital longitude during the individual exposures of the three HST visits analysed here. The width of each box reflects the orbital longitudes covered from start to the end of an exposure. The orbit direction and rotation of the surrounding plasma are shown by the curved arrow. The grey shaded area illustrates Jupiter's shadow. (The direction to the Sun is almost identical to the Earth/HST direction, see solar phase angles in Table 1.)

due to the higher emission intensity and lower background signal. Only one recent study[22] briefly discusses O I 1,304 Å images from individual exposures, mentioning large regions on the disk where $r_\gamma(\mathrm{O\,I}) < 1$.

Here we present evidence for H_2O in Ganymede's atmosphere through a combined analysis of new spectra taken in 2018 by the Cosmic Origins Spectrograph (COS) of HST (HST/COS) together with archival images from HST's Space Telescope Imaging Spectrograph (STIS) from 1998 and 2010.

First, we present two FUV spectra taken with COS in the highest-spectral-resolution mode directly before and during eclipse of Ganymede by Jupiter. With this test, we show that the O atmosphere is optically thin to the 1,304 Å emission, which sets an upper limit on the abundance of O. Analysing the spatial distribution of the O I 1,356 Å and O I 1,304 Å emissions in STIS images, we then found that the emission ratio changes systematically with radial distance to the centre of Ganymede's observed hemisphere and we show that the oxygen intensities and ratios require a substantial abundance of H_2O in the central subsolar region.

Results

COS observed Ganymede with two exposures directly before ingress into Jupiter's shadow (exposure 1) and in total umbral eclipse (exposure 2) (Fig. 1). The observational set-up and data processing are explained in the Methods. The obtained spectra are shown in Fig. 2. If solar resonant scattering by an atomic oxygen atmosphere contributes to the 1,304 Å emission (in addition to electron excitation of O) as suggested in previous studies[11,22], the O I 1,304 Å intensity should drop from exposure 1 to exposure 2 due to the absence of scattered sunlight in the eclipse exposure. Instead of a drop, the measured O I 1,304 Å intensity barely changed from 14.6 ± 1.7 rayleigh (1 rayleigh $\mathrm{R} = \frac{10^6}{4\pi}\frac{\mathrm{photons}}{\mathrm{sr\,cm^2\,s}}$) in sunlight to 15.2 ± 1.0 R in eclipse. In the optically thin limit, the brightness of the scattered signal is the product of the O column density and photon scattering coefficient or g factor, which is 5×10^{-7} photons $\mathrm{s^{-1}}$ for O I 1,304 Å. Setting the limit for a O I 1,304 Å decrease to −1 R (consistent with the 0.6 ± 1.0 R increase from sunlight to eclipse within ~1.5σ), we get an upper limit for the O column density of $2\times10^{12}\,\mathrm{cm^{-2}}$.

The intensity of the semi-forbidden O I 1,356 Å doublet, which can only be excited by electron impacts, decreases from 36.7 ± 2.1 R (in sunlight) to 35.1 ± 1.6 R (in eclipse). This suggests that the auroral (electron) excitation either does not change or slightly decreases between the two exposures, which excludes the possibility that an increase in auroral excitation cancels out and thus masks a potential drop in the resonant scattering of O I 1,304 Å. Furthermore, we have analysed the time series of the intensities over the exposures (Extended Data Fig. 1), which show that the intensities of both oxygen multiplets do not undergo systematic changes but instead seem to be stable throughout the exposures. This stability, as well as the measured line ratios within the O I 1,304 Å triplet, further supports the conclusion that the resonant scattering contribution is negligible (Methods).

The upper limit on O abundance is well below previously estimated values[22] and rules out atomic oxygen as a viable emission source. We next investigated the spatial distribution of r_γ(O I) to gain more insight into the nature of the ratio and, in particular, the difference in the ratio between the trailing and leading hemispheres.

The trailing and leading hemispheres were imaged during three and four HST campaigns, respectively. The two most suitable HST visits for our analysis were selected by considering two criteria: (1) the signal-to-noise ratio in the O I 1,304 Å emission, which is determined by the combined exposure time during low geocorona phase (when HST is on the Earth's nightside); and (2) Ganymede's angular diameter. A diameter of ~1.6″ is optimal for our analysis, because the 2"-wide aperture slit then also captures the region above Ganymede's limb, while the images provide good spatial resolution across the disk (Table 1). The STIS data processing and extraction of the coadded 1,304 Å and 1,356 Å images (Figs. 3b,c and 4b,c) are described in the Methods.

The O I 1,304 Å morphology generally resembles the O I 1,356 Å morphology, as found previously[22]. The image-averaged ratios of $\langle r_\gamma(\mathrm{O\,I})\rangle = 1.8 \pm 0.2$ (trailing) and $\langle r_\gamma(\mathrm{O\,I})\rangle = 2.0 \pm 0.1$ (leading) are also roughly consistent with values previously derived from the same[9] or other[11,22] HST data.

On closer inspection, the O I 1,304 Å emissions become stronger towards the disk centre than the O I 1,356 Å emissions. This is the case on both hemispheres, but is particularly obvious on the trailing hemisphere. We therefore calculated radial intensity profiles for both oxygen emissions and r_γ(O I), with radial bins in steps Δr of 0.2 R_G (Ganymede radius R_G = 2,634 km; Figs. 3d,e and 4d,e).

The emission profiles (Figs. 3d and 4d) reflect the structure of the auroral bands: the near-equator bands on the leading hemisphere result in the highest intensities near radius ~0.3 R_G; the bands closer to the poles on the trailing hemisphere lead to the brightest emissions closer to ~1 R_G.

The ratio profiles (Figs. 3e and 4e), however, are similar on both hemispheres: the ratio peaks close to the limb (~1 R_G) with a maximum value of $r_\gamma(\mathrm{O\,I}) \approx 2.4$, consistent with electron impact on a pure O_2 atmosphere. From these maximum values, r_γ(O I) systematically decreases towards the disk centre as well as towards higher distances above the limb. The mean ratios with uncertainty σ in the disk centres ($r < 0.5\,R_\mathrm{G}$; shaded areas in Figs. 3e and 4e) are $r_\gamma(\mathrm{O\,I}) = 0.97 \pm 0.22$ on the trailing hemisphere and $r_\gamma(\mathrm{O\,I}) = 1.83 \pm 0.16$ on the leading hemisphere. These values differ from a pure O_2 ratio of $r_\gamma(\mathrm{O\,I}) = 2.3$ by 6.0σ and 2.9σ, respectively, requiring another source species. We have searched for other systematic changes in the ratio, such as between the dawn and dusk sides or polar and equatorial regions, but did not find any significant or clear trends.

In previous studies, r_γ(O I) values below 2 were interpreted as indicating higher abundances of atomic oxygen[11,22]. With the upper limit from the COS eclipse observation, the maximum

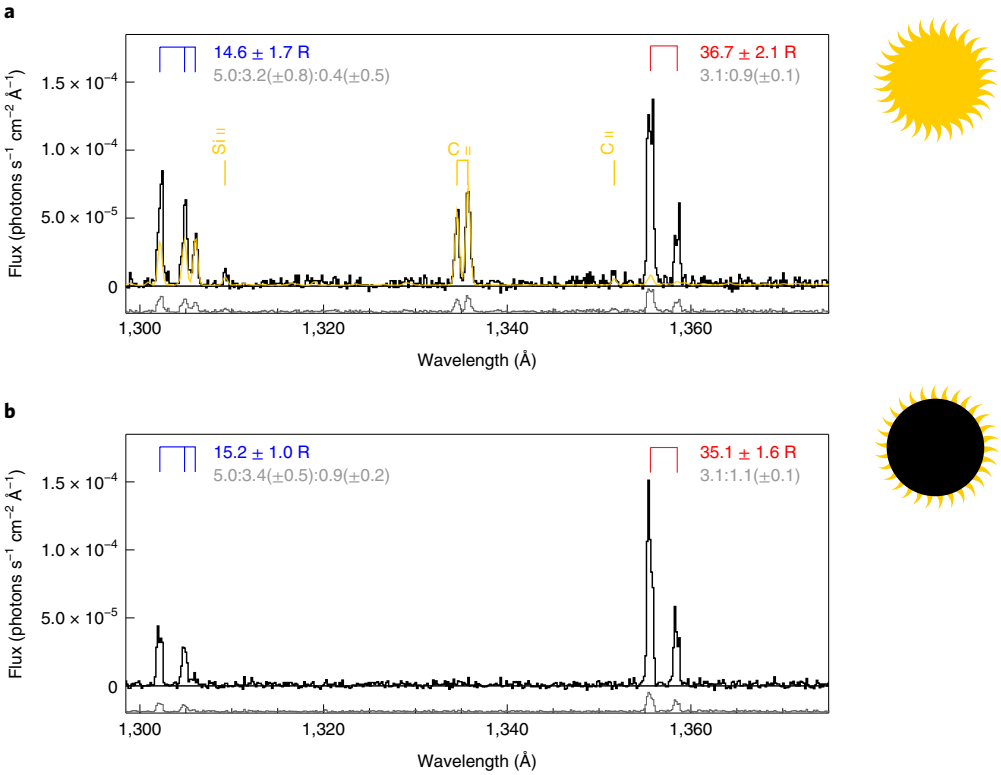

Fig. 2 | COS spectra from exposures 1 and 2. a, Exposure 1 (ld8k2ds1q in Table 1) in sunlight, before ingress to eclipse. **b**, Exposure 2 ((ld8k2ds4q), when Ganymede was eclipsed by Jupiter. The propagated error is shown in grey, at a small negative offset on the *y* axis for readability. A solar spectrum (yellow) is adjusted to the sunlit exposure, with prominent solar lines indicated. COS data are shown in black. The integrated intensities with propagated uncertainties are shown for the atmospheric O I 1,304 Å (blue) and O I 1,356 Å (red) emissions (after subtraction of the solar reflection for exposure 1), and the relative intensities of the individual multiplet lines are given with the brightest lines set to 5.0 and 3.1, respectively. The stability of the O I emissions in and out of eclipse rules out solar scattering as an emission source and limits the O abundance.

Table 1 | Parameters of the HST/COS and HST/STIS observations

HST Campaign	Date	Observed hemisphere	Exposure IDs or number of exposures	Start time (UTC)	End time (UTC)	Total exposure time (s)	Ganymede diameter (arcsec)	Spatial resolution (km per pixel)	Sub-observer CML (° W)	Solar phase angle (°)	System-III longitude (° W)
COS observation											
14634	2018 April 4	sub-Jovian	ld8k2ds1q	14:45	15:16	1,855 (0–1,335)	1.58	n/a	352–354	6.4	233–245
		eclipse	ld8k2ds4q	16:04	16:49	2,680 (0–2,160)		n/a	356–357	6.4	278–298
STIS observations											
7939	1998 October 30	trailing	5 exposures	08:21	13:36	5,136	1.71	76	289–300	8.6	226–45
12244	2010 November 19	leading	5 exposures	20:11	03:00^{+1}	5,515	1.64	79	98–111	10.3	180–43

The superscript +1 indicates that the end time is on the day after the given date. The window of the exposure time used in the COS observations is given in parentheses. n/a, not available; CML, Central meridian (west) longitude on Ganymede's disk. Jupiter's planetocentric longitude facing Ganymede is given by the System-III longitude.

possible abundance of O and the corresponding emission intensity are, however, insufficient to explain the observed ratios (r_γ(O I) < 2) and absolute intensities (20–80 R) near the disk centre.

The minimum O_2 column density in the bound atmosphere required to explain the O I 1,356 Å intensities on the disk was shown to be $N_{O_2} = 1 \times 10^{14}$ cm^{-2} (refs. [9,11,22]). The upper limit on the O column density of $N_O = 2 \times 10^{12}$ cm^{-2} derived earlier hence implies a conservative upper limit for the O/O_2 ratio of 0.02 in the bound atmosphere. The required O/O_2 mixing ratios (shaded areas in Fig. 5b) are, however, considerably larger than 0.02, effectively ruling out atomic oxygen as the constituent that reduces r_γ(O I) in the disk centres.

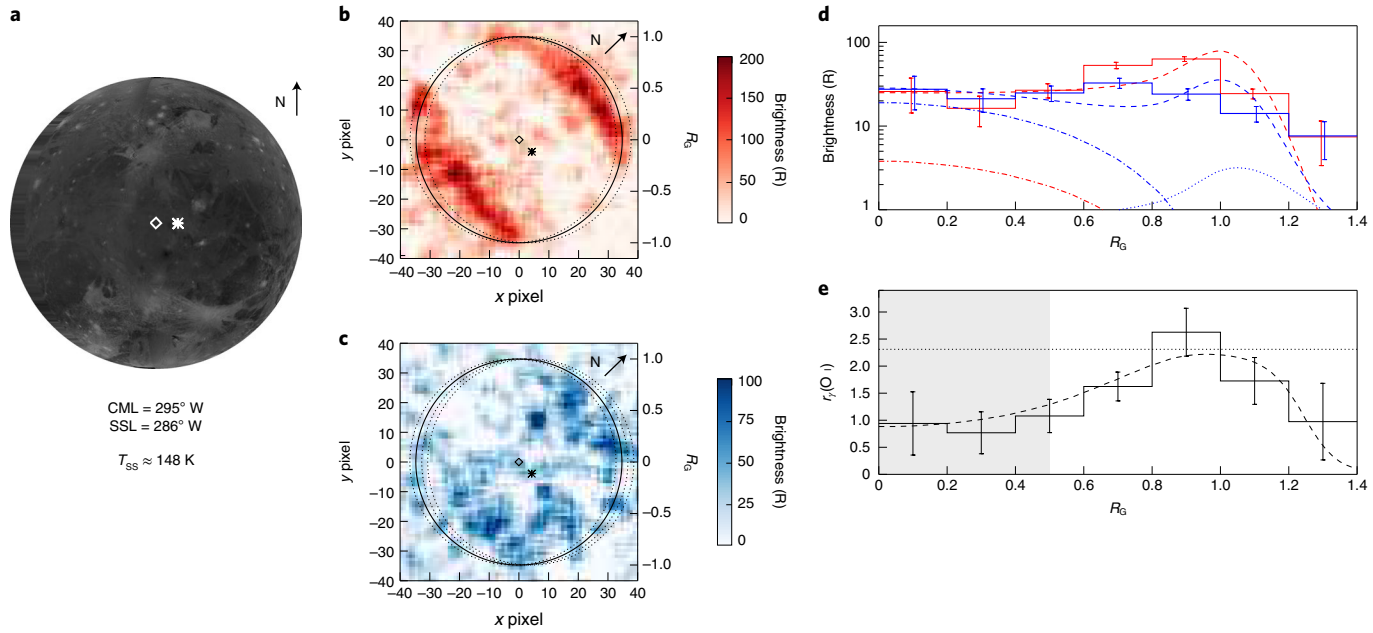

Fig. 3 | Observation of Ganymede's trailing hemisphere. a, Projection of a visible image mosaic[60]. **b**,**c**, HST/STIS images from 1998 of the O I 1,356 Å (**b**) and O I 1,304 Å (**c**) emissions. The arrow shows the direction to Jupiter north (N). The slightly dispersed locations of Ganymede's disk at the individual multiplet lines are shown by dotted circles. Diamonds indicate the disk centre and the asterisks the subsolar point. SSL is the observed subsolar longitude and the given temperature at the subsolar point T_{SS} = 148 K is estimated with a thermal model[36]. **d**, Radial brightness (*I*) profiles of the average O I 1,356 Å (red) and O I 1,304 Å (blue) brightness are plotted as histograms with propagated uncertainties (error bars) within concentric rings from the disk centre out to ≥1.4 R_G. Radial emissions profiles of the simulated aurora with the assumed model atmosphere are shown for the total modelled intensity (dashed) and for the individual contributions from O (dotted), and H_2O (dash-dotted). The O_2-only model can be inferred from the differences between these models. **e**, The profile of r_γ(O I) for HST data (histogram with error bars of the propagated uncertainties) agrees with the ratio of O_2 (dotted horizontal line) only near the limb, but is in good agreement with the $O_2 + O + H_2O$ atmosphere model (dashed) at all radial distances. The derived column density ratio N_{H_2O}/N_{O_2} in the centre region (shaded grey) is 12–32.

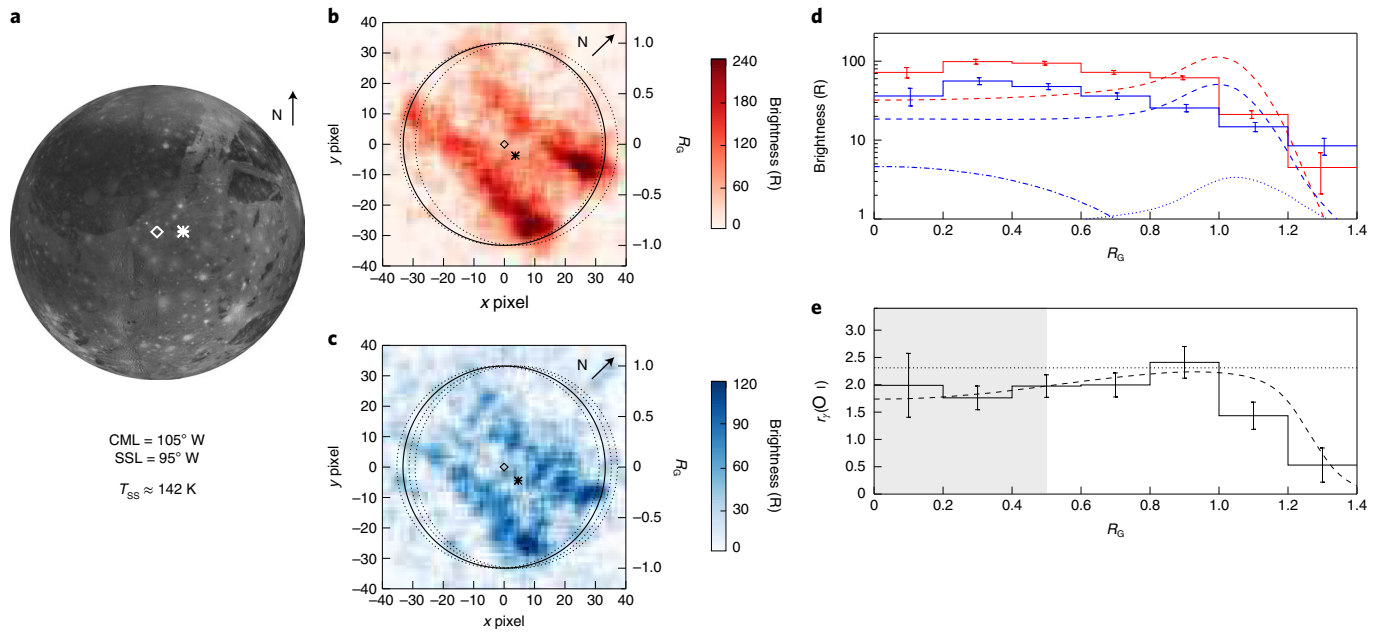

Fig. 4 | Observation of Ganymede's leading hemisphere. a, Projection of a visible image mosiac. **b**,**c**, HST imageas of the O I emissions. **d**, Radial brightness profiles of the observed (histogram) and modelled intensities (dashed: total model; dotted: O only; dash-dotted: H_2O only). **e**, profiles of r_γ(O I) for observations and models. For details on the panels see caption of Fig. 3. The estimated surface temperature (142 K) is lower as the albedo is higher. The measured profile of the line ratio is qualitatively similar to the trailing hemisphere but decreases only to ~1.8 on the disk. The derived column density ratio N_{H_2O}/N_{O_2} (bottom) is accordingly lower (2–5), as expected for the colder surface if sublimation is the source.

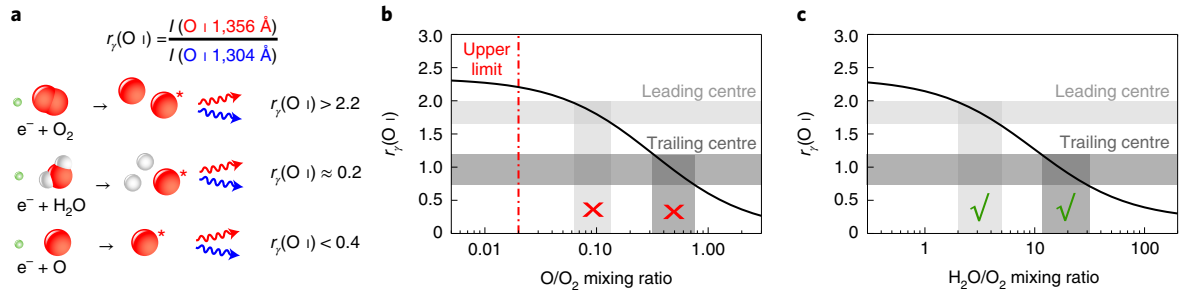

Fig. 5 | The oxygen emission ratio is diagnostic of the atmospheric composition. a, Schematic showing how r_γ(O I) is diagnostic of the atmospheric composition via the relative excitation and thus emission rates[12,14,16,61]. Electron impact produces electronically excited oxygen atoms (indicated by the asterisk) with different rates for the levels of the two emission mulitplets. **b**,**c**, r_γ(O I) as a function of the mixing ratios of O (**b**) and H_2O (**c**) in an O_2 atmosphere for electron impact only (solid). An electron temperature of $T_e = 100$ eV is assumed but the relative exciting ratios and thus mixing ratios are similar for reasonable values between 10 eV and 200 eV. The grey shaded areas indicate the mean ratios $\pm 1\sigma$ in the disk centre regions ($<0.5\,R_G$) and the corresponding mixing ratio ranges. While the inferred upper limit on the O/O_2 ratio (dashed-dotted red line in **b**) precludes atomic oxygen (illustrated by the red crosses), high H_2O/O_2 ratios can explain the r_γ(O I) values in the centre regions (green ticks). Resonant scattering of O I 1,304 Å by O is not included as its contribution was shown to be negligible in our eclipse test.

Similar to atomic oxygen, electron impact dissociation of water vapour (H_2O) produces considerably stronger O I 1,304 Å emissions (Fig. 5a). The FUV oxygen ratio was recently used as diagnostic to distinguish between O_2, H_2O and CO_2 in the gas environment of comet 67P/C-G in a series of studies (for example, refs. [23,24]) as well as to support the detection of localized H_2O aurora at Europa[25]. The total oxygen emission rates for H_2O are about an order of magnitude lower than those for O_2 (refs. [14,16]). The H_2O abundance must therefore clearly exceed the O_2 abundance to effectively reduce r_γ(O I). Indeed, H_2O/O_2 mixing ratios in the range of 12–32 (trailing hemisphere) and 2–5 (leading hemisphere) are consistent with the observed centre emission ratios (Fig. 5c), implying that the atmosphere in the disk centre regions is dominated by H_2O.

In the region above the limb ($r > 1.2\,R_G$), where r_γ(O I) also drops below 2, the absolute intensities are lower (<10 R) and the O_2 abundance is probably also lower. Here, contributions from O (and a higher O/O_2 mixing ratio) in the extended exosphere can possibly explain the lower oxygen emission ratio, similar to Europa[17]. Given the overall low emission intensities there, even small abundances of O near our upper limit would be sufficient to reduce r_γ(O I). The two different constituents lowering r_γ(O I) in the two different regions (H_2O near the centre, O in the above-limb region) is also a consistent explanation for the particular radial profiles in the emission ratio, with a peak near the limb and the two separate minima.

We simulated the global electron-excited oxygen emissions for a model O_2–O–H_2O atmosphere (Methods). The goal of the simulations was to produce emission ratio profiles consistent with the observed profile on the basis of simplified but reasonable neutral and electron properties. In particular, we assumed a global O_2 atmosphere with a vertical column density of $N_{O_2} = 2.8 \times 10^{14}\ \mathrm{cm}^{-2}$ everywhere and an H_2O atmosphere strongly concentrated around the subsolar point. The assumption of a global O_2 abundance is supported by the global presence of the 1,356 Å emissions[21], which originate almost entirely from O_2 (Extended Data Fig. 2). Potential asymmetries in the global O_2 atmosphere, which were recently proposed to be present between the dawn and dusk limb[4,26], do not affect the oxygen emission ratio and are negligible for our analysis. The surface H_2O density at the subsolar point was then adjusted to match the measured oxygen emission ratios in the disk centre regions on the two hemispheres. The model line-of-sight column densities for O_2, O and H_2O for the trailing hemisphere observation are shown in Extended Data Fig. 3.

We refrain from stating uncertainty ranges on absolute abundances assumed in the model, which would mostly reflect the uncertainty in the poorly constrained electron properties[22]. The assumed model scenario represents a reasonable O_2 density in Ganymede's atmosphere and a corresponding electron excitation potential consistent with the measured image-averaged oxygen intensities. Other scenarios such as a substantially higher electron excitation potential (implying lower atmospheric abundances[27] or an overall denser atmosphere, as recently suggested[28]) and reduced electron excitation are also possible. Note, however, that the H_2O/O_2 ratio ranges derived above are much less sensitive to electron properties (independent of electron density) and thus more reliable constraints.

The simulation results show that contributions from H_2O and O are marginal for the total (image-averaged) O I 1,356 Å intensity, which almost entirely originates from (and thus directly constrains) the abundance of O_2 (Extended Data Fig. 2). The contributions from H_2O and O to the O I 1,304 Å emissions averaged over the image, in contrast, are about 15% and 10%, affecting the oxygen emission ratio and the radial ratio profiles (Figs. 3e and 4e).

The simulated emission profiles (Figs. 3d and 4d) mostly reflect limb brightening from the line-of-sight integration of the global O_2 atmosphere. The simulated oxygen ratio profiles, however, reflect the mixing ratios and thus the H_2O atmosphere around the subsolar point and the extended O exosphere at higher altitudes above the limb.

We note that in the bins of the largest radial distance ($r > 1.2\,R_G$), the observed emissions at both oxygen lines seem to be systematically higher than the vanishing emission in the simulation profiles. This difference might be related to an additional radially extended part of the exosphere[28,29], which was not included here to keep our model simple.

The simulated r_γ(O I) profiles are consistent with the observed profiles on both hemispheres. The maximum is in the radial bins at or just inside $1\,R_G$ in all cases, which is the region where contributions from H_2O and O to the O I 1,304 Å emissions (dash-dotted and dotted lines in Figs. 3 and 4) are lowest. Towards the disk centre, the H_2O column density and hence the emission from H_2O increases, reducing the resulting oxygen emission ratio. At larger radial distances above the limb, the higher abundance of O in the extended atmosphere leads to higher O I 1,304 Å emission than O I 1,356 Å emission, and thus to the decrease in r_γ(O I).

Besides oxygen emission, electron impact on H_2O produces H Lyman α emission with an estimated intensity of about 200 R. In the available data, however, this is indistinguishable from spatially variable surface reflections at Lyman α (ref. [10]).

Discussion

The low oxygen emission ratios in the centre of Ganymede's observed hemispheres are consistent with a locally H_2O-dominated

atmosphere. With phase angles of around 10° (Table 1), the disk centres are close to the subsolar points (diamonds and asterisks in Figs. 3 and 4). A viable source for H_2O in Ganymede's atmosphere could be sublimation in the low-latitude subsolar regions[30], where an H_2O-dominated atmosphere was predicted by atmospheric models[2,4,6]. Our derived H_2O mixing ratios are in agreement with these predictions. While previously detected tenuous atmospheres around icy moons in the outer Solar System were consistent with surface sputtering (or active outgassing) as the source of the neutral species[31–33], our analysis provides evidence for a sublimated atmosphere on an icy moon in the outer Solar System. Water ice sublimation at heliocentric distances of ~5 au has been indirectly observed through photolysis products at comets (for example, ref. [34]). A tentative direct measurement of H_2O at comet C/2006 W3 at 5 au was interpreted to originate from sublimation from small ice-bearing grains[35].

Surface temperatures on Ganymede's dayside trailing and leading hemispheres of ~148 K and ~142 K were estimated by a thermal model taking into account albedo and the thermal inertia of the surface[36], consistent with observations[3]. The vapour pressure above pure ice[37] at these temperatures converts to H_2O densities of 1.7×10^9 cm^{-3} on the trailing hemisphere subsolar point and density about sixfold lower (3.1×10^8 cm^{-3}) on the leading hemisphere, using the ideal gas law. This difference between the trailing and leading hemispheres is remarkably similar to the difference found in our data: the emission ratios also suggest an approximately sixfold higher H_2O/O_2 ratio above the central trailing hemisphere (Figs. 3 and 4).

With an assumed scale height of 50 km for the modelled H_2O atmosphere (close to the nominal scale height at 140 K), the model surface densities are 1.2×10^9 cm^{-3} at the central trailing hemisphere and 2.0×10^8 cm^{-3} at the central leading hemisphere. These model surface densities correspond to ~71% (trailing) and ~65% (leading) of the theoretical values for pure ice stated above. Ganymede's surface reflectance spectra were shown to be consistent with both a homogeneous surface material consisting of 90% ice and a segregated surface, with regions of pure ice (50% of the area) and ice-free regions covered by dark deposits[38]. Recent studies suggest that the abundance of darkening material relative to ice is higher near the equator and particularly on the trailing hemisphere[39,40], which apparently does not impede (or barely impedes) sublimation there. The vapour density fractions of 71% and 65% of the values for pure ice found for the two hemispheres are suggestive of a relatively high ice fraction; the various measurements and model uncertainties (particularly the uncertainty of the electron properties and the sensitivity of the vapour pressure to small temperature changes) prevent further conclusions. Recent analysis of Ganymede's FUV reflectance also suggests that the surface ice contains a small fraction (<1% by volume) of UV-absorbing impurities[41], which may modify the expected sublimation rate. Sublimation and subsequent volatile transport are also likely to affect the geological landforms on Ganymede leading to, for example, the formation of specific dark features[42,43].

At the terminator, the temperature drops below 100 K (refs. [3,44]) and the H_2O vapour pressure is negligible, consistent with $r_\gamma(\mathrm{O\,I}) > 2$ and pure O_2 near the limb. Thus, our results suggest that Ganymede's atmosphere possesses a pronounced day/night asymmetry. There seems to be a density difference from the subsolar point to the terminator (and nightside) by more than an order of magnitude, particularly when the trailing hemisphere is illuminated. If Ganymede's atmosphere is collisional, this difference might lead to atmospheric day/night winds, which are also expected to be present at Io[45]. Such asymmetries also fundamentally affect the space plasma and magnetospheric environment and need to be taken into account in numerical simulations (for example, refs. [28,46–48]) and future data analysis for a comprehensive understanding of the Ganymede system.

The Jupiter Icy Moons Explorer (JUICE) mission of the European Space Agency will investigate Ganymede in great detail with its eleven science instruments during several flybys in the first mission phase (expected for the period 2031–2034) and finally from orbit around the moon (from 2034). Several science instruments are equipped to measure Ganymede's neutral gas environment and particularly the H_2O abundance by remote sensing of UV, optical, infrared and submillimetre emissions[49,50], as well as in situ sensing with the neutral particle detector.

The JUICE mission plan is to orbit Ganymede for at least 280 days, in a variety of orbits including circular phases at altitudes of ~5,000 km and ~500 km. During these periods, it is planned that the JUICE UV spectrograph (UVS) instrument will map the location, brightness and altitude distribution of OCFB emissions of O I 1,356 Å and O I 1,304 Å over a wide range of longitudes. For the planned surface reflectance mapping measurements at far-UV wavelengths using the 1,650 Å absorption edge feature[41,51], it will be useful to search for latitudinal trends associated with the transport of water vapour away from the subsolar point and to determine whether the transport extends to persistently shaded regions near Ganymede's poles.

The atmospheric and surface UVS measurements will be combined with observations of both the surface and atmosphere by other JUICE instruments to determine the sources and sinks of Ganymede's exosphere and ionosphere. Our results place observational constraints on the contribution of sublimation to the atmosphere, and provide the JUICE instrument teams with valuable information that may be used to refine their observation plans to optimize the use of the limited spacecraft power and telemetry resources.

Methods

Data and processing. *HST/COS spectra.* The two analysed HST/COS exposures were obtained in April 2018 (Table 1) during two consecutive HST orbits with the G130M grating and a central wavelength of 1,291 Å. The wavelength range of 1,290–1,430 Å on the COS detector segment A includes the emissions from the oxygen triplet around 1,304 Å and the doublet at 1,356 Å. The individual multiplet lines (1,302.7 Å, 1,304.9 Å, 1,306.0 Å/1,355.6 Å, 1,358.8 Å) are spectrally resolved at a nominal resolution of 0.17 Å per resolution element. We discuss the measured multiplet line ratios briefly at the end of this section. Due to acquisition at the start of the first HST orbit, exposure 1 (ld8k2ds1q) is shorter, while the entire second HST orbit was used for science exposure 2 (ld8k2ds4q) (Table 1). Between the first and second exposures, Ganymede entered the umbral shadow of Jupiter (at 15:27 UTC on 2018 April 4).

Ganymede seems to be well centred in the 2.5"-wide aperture, as revealed by a Gaussian fit to the integrated signal along the spatial (y) detector axis in the first exposure. The fit to the signal, which is dominated by the reflected sunlight, has a peak near the nominal centre and a full width of 1.7", close to Ganymede's angular diameter (Table 1). As the pointing of HST is stable, Ganymede should be similarly centred in the aperture in the second exposure.

Extended Data Fig. 1 shows the temporal evolution of the detector count rates around the two oxygen emissions at 1,304 Å and 1,356 Å. Towards the end of both exposures, the O I 1,304 Å signal increases sharply due to scattered light from the Earth's oxygen geocorona when HST approaches the terminator region. We hence reduced the exposure times by 520 s each (Table 1). Apart from the O I 1,304 Å increase due to the geocoronal signal, the count rates seem to be stable for both lines and in both exposures. The systematically higher O I 1,304 Å count rate in exposure 1 when compared with exposure 2 originates from the surface reflection in sunlight, which was removed in a subsequent processing step.

The detected counts were then integrated along the spatial axis and over the reduced exposure time to obtain a spectrum for each exposure. Using the tabulated detector sensitivity, the count rate (counts per exposure time) was converted to the photon flux, shown in Fig. 2. The propagated uncertainties (which include the Poisson noise and uncertainties in the correction of the background signal and (in the case of exposure 1) subtracted solar flux) are shown per spectral bin in grey. The complete spectrum of the first exposure (Fig. 2a) contains several solar lines, with the C II doublet near 1,335 Å being most prominent. To remove the reflected sunlight, we applied the same method and data as used and discussed in previous works[18,52]. The adjusted and fitted spectrum from the Solar Radiation and Climate Experiment/Solar Stellar Irradiance Comparison Experiment (SORCE/SOLSTICE) is shown in orange and matches both the C II and Si IV lines well. As Ganymede was in total umbral eclipse throughout the second exposure, surface reflections are not present.

We calculated total intensities measured at O I 1,304 Å and O I 1,356 Å lines and normalized them to the area of Ganymede's disk (in analogy to ref. [11]). The resulting disk-averaged intensities are shown in Fig. 2 along with the relative intensities of the three (O I 1,304 Å) and two (O I 1,356 Å) multiplet lines. The obtained intensities are identical in the two exposures for both oxygen emissions within their respective propagated uncertainties. The resulting ratio is slightly higher in the first (r_γ(O I) = 2.5 ± 0.3) than in the second exposure (r_γ(O I) = 2.3 ± 0.2), although this difference is not significant either.

Oxygen multiplet line ratios in COS data. The COS data also resolves the multiplet lines of both oxygen emissions. The multiplet ratios are diagnostic for the source processes and optical thickness effects, and we therefore discuss the results here briefly.

The ratio of the three multiplet lines of the 1,304 Å emissions is in both exposures (Fig. 2, light grey) consistent with the theoretical relative line strength for a collisionless and optically thin atmosphere. The ^3S–^3P transitions have different ground states but originate from the same excited upper state ($3S$, $J = 1$), and the ratios in the optically thin case relate to the Einstein A coefficients; that is, 1,302.2 Å:1,304.9 Å:1,306.0 Å = 5:3:1 (ref. [53]). If there is a source of emission at high optical depth in a very optically thick medium (as for the chromosphere and transition region of the Sun), then the multiple photon scattering cancels out the effect, leading to similar (or even slightly reversed) relative intensities for the three lines[54].

In a marginally optically thick medium, there might be small deviations from the 5:3:1 ratio. Since resonance scattering involves partial frequency redistribution, there is a different scattering phase function for each line in the triplet depending on the relative weight of the Rayleigh phase function. This can lead to a change in the line ratio for a directional source flux, as for the solar flux[55]. For the small solar phase angle during the COS observations of 7°, a slightly different multiplet ratio of 1,302.2 Å:1,304.9 Å:1,306.0 Å = 5:3.4:1.5 is theoretically expected[55] for only solar resonant scattering. Hence, the very faint line at 1,306.0 Å in the sunlit exposure (multiplet ratio in Fig. 2b) would not be consistent with a dominating resonant scattering signal. However, this is only a weak diagnostic, as the differences in the multiplet ratio for resonant scattering and (isotropic) electron excitation are small.

The obtained ratios for the O I 1,356 Å doublet (Fig. 2, light grey) are similarly in agreement for both exposures with the theoretical ratio of 1,355.6 Å:1,358.0 Å = 3.1:1.0 (ref. [53]).

HST/STIS spectral images. FUV spectral images with the G140L grating and the 52" × 2" slit that include maps of Ganymede's oxygen emissions were taken within six HST campaigns (IDs 7939, 8224, 9296, 12244, 13328 and 14634). We analysed the spatial distribution of the O I 1,304 Å and O I 1,356 Å emissions with image pairs from two representative HST visits for the trailing and leading hemispheres, selected after the criteria as described in the main text.

We combined all low-geocorona exposures—five from the 1998 trailing hemisphere visit (IDs o53k01010, o53k01020, o53k01040, o53k01060 and o53k01080) and five from the 2010 leading hemisphere visit (IDs objy03020, objy03040, objy03060, objy03080 and objy030a0)—for a superposition image with improved signal-to-noise ratio. We then followed a standard processing pipeline for correcting the detector images for background and surface reflection signals, see ref. [56] or ref. [17] for details. We updated the method for subtracting solar surface reflections in two aspects: because lower-resolution spectra slightly smear the spectral trace, we used the high-resolution spectra from the SORCE/SOLSTICE instrument[57] and adjusted them to the STIS G140L resolution (for the 1998 visit only a UARS/SOLSTICE spectrum with lower resolution is available). Furthermore, we took into account the longitudinal variation of the solar flux in the selection of the UARS/SOLSTICE data. We used the SOLSTICE spectrum from the day closest to the HST observation day but when the solar longitude facing Earth matched the Jupiter-facing longitude from the day of the observation.

After correction for background and solar reflection, 80 × 80 pixel images (over the full slit width) containing the oxygen emission images centred on the spectral axis at 1,303.5 Å and 1,356.3 Å were extracted from the spectral detector images and converted to rayleigh. The analysis was carried out in the native detector frame and original pixel resolution without smoothing. For the displays in Figs. 3 and 4, the images were smoothed with a 5 × 5 pixel boxcar function but not rotated to a common frame. All analysis was carried out with the original data (no binning or smoothing applied). The propagated uncertainties (which include the Poisson noise and uncertainties in the correction of the background signal and subtracted solar flux (in the case of exposure 1)) are shown per spectral bin in grey. Statistical uncertainties based on Poisson statistics in each image pixel were propagated through this processing (that is, the uncertainties from the correction of the background signal and subtracted solar flux added) and converted to rayleigh.

We calculated image-average emission intensities taking into account all pixels within 1.25 R_G around the disk centre and normalizing it to the area of these pixels (that is, not to the area of Ganymede's disk as done for spectral observations without spatial information). These image-averaged intensities are given in Extended Data Fig. 2, along with the modelled intensities from each atmospheric constituent and the total atmosphere.

Modelling. The goal was to reproduce the emission intensities as well as the radial line ratio profiles with a simple model with as few assumptions and parameters as possible for both the atmospheric distribution and the electron properties.

For the neutral gas distributions, we assumed a global, exponentially decreasing atmospheric O_2 density with a fixed scale height of 100 km and a surface density of $n_{O_2,0}$. This scale height is on the order of the spatial resolution of the STIS images (Fig. 1), meaning that the density above the limb as seen by STIS decreases to 1/e of the maximum over 1–2 pixels. As discussed above, the global O_2 abundance is supported by the fact that O I 1,356 Å emissions are observed across all longitudes. The assumption is also justified by the long lifetime or residence time of O_2 in the atmosphere, which is on the order of Ganymede's orbital period[2,4].

Atomic O is probably produced primarily through the dissociation of the molecular atmosphere (with excess energy), suggesting a higher temperature and a more gradual radial decrease than for mainly surface-derived species. We thus assumed a larger scale height of 400 km. With the derived upper limit on column density, we get a fixed surface density for O of $n_{O,0} = 5 \times 10^4$ cm^{-3}.

As a third constituent, we assumed an H_2O abundance from sublimation concentrated around the disk centre (the subsolar point) given by

$$n_{H_2O}(h, \alpha) = n_{H_2O,0} \cos^6(\alpha) \exp\left(-\frac{h}{H_{H_2O}}\right), \quad (1)$$

where $n_{H_2O,0}$ is the density at the surface, h the altitude above the surface, α the angle to the disk centre and H_{H_2O} the scale height. The nominal scale height for H_2O at Ganymede's surface at temperature $T = 140$ K is 48 km, and we hence assumed a scale height of 50 km. (Owing to the concentration of H_2O near the disk centre and the absence of H_2O near the observed limb, the H_2O column density derived from the emission intensity is essentially independent of the scale height.) The approximated cosine to the sixth dependence on the angle to the subsolar point (α) roughly reproduces the steep gradient near ($\alpha = 45°$) found in models (see, for example, fig. 3 of ref. [2]). We then produced column density maps for each of the three species by integrating along the line of sight with the subsolar point on the disk centre (Extended Data Fig. 3).

To compute the emission intensities, we then needed to make assumptions for the electron population that excites the emissions. Ganymede's aurora is suggested to be excited by an accelerated population of electrons with T_e between 75 eV and 300 eV (ref. [27]). There are no measurements or independent constraints available for T_e in Ganymede's environment. For our model estimations, we assumed one Maxwellian electron population at 100 eV to excite the oxygen emissions (which is also the temperature where the 1,356 Å yield from H_2O was measured[14]).

For the density of the electrons, we considered the extent of the auroral band emissions seen on the two hemispheres and the related total intensities. For the trailing hemisphere observations, we assumed an electron density of 20 cm^{-3} to roughly match the observed image-averaged O I 1,356 Å intensity at the assumed O_2 abundance. On the leading hemisphere, the observed auroral intensities are higher due to the long equatorial auroral bands, and we set the electron density to 30 cm^{-3}, again matching the observed image-averaged O I 1,356 Å intensity. These densities are slightly higher than the electron density in Jupiter's magnetosphere near Ganymede[58], but are lower than the peak densities measured by Galileo near closest approach to Ganymede[29].

The local volumetric emission from electron (dissociative) excitation was calculated by multiplying the local neutral density with the constant electron density and emission rates. The emission rates are derived as an integral over the Maxwell–Boltzmann distribution, the electron velocity and the energy-dependent cross-sections for the collision of the exciting electrons with the neutral species. Cross-sections were taken from laboratory measurements of the considered species[12–14,16]. For atomic oxygen, contributions from cascades from higher states to the upper levels were approximated. We note that electron impacts on H_2O can produce excited neutral oxygen atoms via several dissociation channels[14]. Finally, the two-dimensional emission pattern was given by the line-of-sight integral over the local intensities.

Given that acceleration processes are probably required to produce the observed emissions[27], the electron distribution can be highly inhomogeneous with regions of hot (accelerated) electrons and regions of electrons with lower temperature (but possibly higher density). Our assumption of a homogeneous plasma follows previous approaches[9,11] and the results for the relative H_2O abundance should be relatively insensitive to the exact electron properties. Dissociative excitation of O_2 consistently produces an emission ratio of r_γ(O I) > 2.2 in the range of possible electron temperatures, and the emission ratios for excitation of O and H_2O are similarly consistently r_γ(O I) ≪ 1. Hence, while the absolute neutral abundances depend on the loosely constrained electron properties, the required relative abundances and thus mixing ratios of O and H_2O do not strongly depend on the assumed electron temperature or density.

Resonant scattering by O was considered using the estimations from ref. [18] (see their fig. 9). The line-of-sight O column density near the limb locally exceeds the nominal derived upper limit, but the average column density and thus scattering contribution is ~1 R in both cases, and thus in agreement with the COS results.

The simulated aurora images were degraded to the STIS spatial resolution and smoothed to account for the STIS point spread function and the offset of

the individual multiplet lines from the line centre (for details of the production of synthetic STIS images see our earlier work[59]). We then adjusted the surface densities for H_2O to match the O I 1,304 Å intensities and resulting line ratios in the observations. From the simulated and degraded images, we then produced radial profiles for the oxygen emissions and for the resulting oxygen emission ratio, in analogy to the derivation of the observed profiles but with smaller radial bins.

Data availability

All used Hubble Space Telescope data are publicly available at the Mikulski Archive for Space Telescopes (http://archive.stsci.edu/hst/). Source data are provided with this paper.

Received: 8 December 2020; Accepted: 4 June 2021;
Published online: 26 July 2021

References

1. Johnson, R. E., Lanzerotti, L. J., Brown, W. L. & Armstrong, T. P. Erosion of Galilean satellite surfaces by Jovian magnetosphere particles. *Science* **212**, 1027–1030 (1981).
2. Marconi, M. L. A kinetic model of Ganymede's atmosphere. *Icarus* **190**, 155–174 (2007).
3. Orton, G. S., Spencer, J. R., Travis, L. D., Martin, T. Z. & Tamppari, L. K. Galileo photopolarimeter-radiometer observations of Jupiter and the Galilean satellites. *Science* **274**, 389–391 (1996).
4. Leblanc, F. et al. On the orbital variability of Ganymede's atmosphere. *Icarus* **293**, 185–198 (2017).
5. Turc, L., Leclercq, L., Leblanc, F., Modolo, R. & Chaufray, J.-Y. Modelling Ganymede's neutral environment: a 3D test-particle simulation. *Icarus* **229**, 157–169 (2014).
6. Plainaki, C. et al. The H_2O and O_2 exospheres of Ganymede: the result of a complex interaction between the Jovian magnetospheric ions and the icy moon. *Icarus* **245**, 306–319 (2015).
7. Shematovich, V. I. Neutral atmosphere near the icy surface of Jupiter's moon Ganymede. *Solar Syst. Res.* **50**, 262–280 (2016).
8. Barth, C. A. et al. Galileo ultraviolet spectrometer observations of atomic hydrogen in the atmosphere at Ganymede. *Geophys. Res. Lett.* **24**, 2147–2150 (1997).
9. Feldman, P. D. et al. HST/STIS ultraviolet imaging of polar aurora on Ganymede. *Astrophys. J.* **535**, 1085–1090 (2000).
10. Alday, J. et al. New constraints on Ganymede's hydrogen corona: analysis of Lyman-α emissions observed by HST/STIS between 1998 and 2014. *Planet. Space Sci.* **148**, 35–44 (2017).
11. Hall, D. T., Feldman, P. D., McGrath, M. A. & Strobel, D. F. The far-ultraviolet oxygen airglow of Europa and Ganymede. *Astrophys. J.* **499**, 475–481 (1998).
12. Doering, J. P. & Gulcicek, E. E. Absolute differential and integral electron excitation cross sections for atomic oxygen. VII—the $^3P \rightarrow {}^1D$ and $^3P \rightarrow {}^1S$ transitions from 4.0 to 30 eV. *J. Geophys. Res.* **94**, 1541–1546 (1989).
13. Johnson, P. V., Kanik, I., Shemansky, D. E. & Liu, X. Electron-impact cross sections of atomic oxygen. *J. Phys. B* **36**, 3203–3218 (2003).
14. Makarov, O. P. et al. Kinetic energy distributions and line profile measurements of dissociation products of water upon electron impact. *J. Geophys. Res.* **109**, A09303 (2004).
15. Hall, D. T., Strobel, D. F., Feldman, P. D., McGrath, M. A. & Weaver, H. A. Detection of an oxygen atmosphere on Jupiter's moon Europa. *Nature* **373**, 677–679 (1995).
16. Kanik, I. et al. Electron impact dissociative excitation of O_2: 2. Absolute emission cross sections of the OI(130.4 nm) and OI(135.6 nm) lines. *J. Geophys. Res.* **108**, 5126 (2003).
17. Roth, L. et al. Europa's far ultraviolet oxygen aurora from a comprehensive set of HST observations. *J. Geophys. Res. Space Phys.* **121**, 2143–2170 (2016).
18. Cunningham, N. J. et al. Detection of Callisto's oxygen atmosphere with the Hubble Space Telescope. *Icarus* **254**, 178–189 (2015).
19. McGrath, M. A. et al. Aurora on Ganymede. *J. Geophys. Res. Space Phys.* **118**, 2043–2054 (2013).
20. Saur, J. et al. The search for a subsurface ocean in Ganymede with Hubble Space Telescope observations of its auroral ovals. *J. Geophys. Res. Space Phys.* **120**, 1715–1737 (2015).
21. Musacchio, F. et al. Morphology of Ganymede's FUV auroral ovals. *J. Geophys. Res. Space Phys.* **122**, 2855–2876 (2017).
22. Molyneux, P. M. et al. Hubble Space Telescope observations of variations in Ganymede's oxygen atmosphere and aurora. *J. Geophys. Res. Space Phys.* **123**, 3777–3793 (2018).
23. Feldman, P. D. et al. Measurements of the near-nucleus coma of comet 67P/Churyumov-Gerasimenko with the Alice far-ultraviolet spectrograph on Rosetta. *Astron. Astrophys.* **583**, A8 (2015).
24. Paul, D. FUV spectral signatures of molecules and the evolution of the gaseous coma of comet 67P/Churyumov-Gerasimenko. *Astron. J.* **155**, 9 (2018).
25. Roth, L. et al. Transient water vapor at Europa's South Pole. *Science* **343**, 171–174 (2014).
26. Oza, A. V., Johnson, R. E. & Leblanc, François Dusk/dawn atmospheric asymmetries on tidally-locked satellites: O_2 at Europa. *Icarus* **305**, 50–55 (2018).
27. Eviatar, A. et al. Excitation of the Ganymede ultraviolet aurora. *Astrophys. J.* **555**, 1013–1019 (2001).
28. Carnielli, G. et al. Constraining Ganymede's neutral and plasma environments through simulations of its ionosphere and Galileo observations. *Icarus* **343**, 113691 (2020).
29. Eviatar, A., Vasyliūnas, V. M. & Gurnett, D. A. The ionosphere of Ganymede. *Planet. Space Sci.* **49**, 327–336 (2001).
30. Squyres, S. W. Surface temperatures and retention of H_2O frost on Ganymede and Callisto. *Icarus* **44**, 502–510 (1980).
31. McGrath, M. A., Lellouch, E., Strobel, D. F., Feldman, P. D. & Johnson, R. E. in *Jupiter: The Planet, Satellites and Magnetosphere* (eds Bagenal, F. et al.) 457–483 (Cambridge Univ. Press, 2004).
32. Teolis, B., Tokar, R., Cassidy, T., Khurana, K. & Nordheim, T. in *Enceladus and the Icy Moons of Saturn* (eds Schenk, P. M. et al.) 361–384 (Univ. Arizona Press, 2018).
33. Paganini, L. et al. A measurement of water vapour amid a largely quiescent environment on Europa. *Nat. Astron.* **489**, 266–272 (2019).
34. Weaver, H. A., Feldman, P. D., A'Hearn, M. F. & Arpigny, C. The activity and size of the nucleus of comet Hale-Bopp (C/1995 O1). *Science* **275**, 1900–1904 (1997).
35. de Val-Borro, M. et al. Herschel observations of gas and dust in comet C/2006 W3 (Christensen) at 5 AU from the Sun. *Astron. Astrophys.* **564**, A124 (2014).
36. Spencer, J. R., Lebofsky, L. A. & Sykes, M. V. Systematic biases in radiometric diameter determinations. *Icarus* **78**, 337–354 (1989).
37. Feistel, R. & Wagner, W. Sublimation pressure and sublimation enthalpy of H_2O ice Ih between 0 and 273.16 K. *Geochim. Cosmochim. Acta* **71**, 36–45 (2007).
38. Spencer, J. R. Icy Galilean satellite reflectance spectra: less ice on Ganymede and Callisto? *Icarus* **70**, 99–110 (1987).
39. Ligier, N. et al. Surface composition and properties of Ganymede: updates from ground-based observations with the near-infrared imaging spectrometer SINFONI/VLT/ESO. *Icarus* **333**, 496–515 (2019).
40. Mura, A. et al. Infrared observations of ganymede from from Juno/Jovian infrared auroral mapper. *J. Geophys. Res. Planets* **125**, e2020JE006508 (2020).
41. Molyneux, P. M., Nichols, J. D., Becker, T. M., Raut, U. & Retherford, K. D. Ganymede's far-ultraviolet reflectance: constraining impurities in the surface ice. *J. Geophys. Res. Planets* **125**, e2020JE006476 (2020).
42. Prockter, L. M. et al. Dark terrain on Ganymede: geological mapping and interpretation of Galileo Regio at high resolution. *Icarus* **135**, 317–344 (1998).
43. Mangold, N. Ice sublimation as a geomorphic process: a planetary perspective. *Geomorphology* **126**, 1–17 (2011).
44. de Kleer, K. et al. Ganymede's surface properties from millimeter and infrared thermal emission. *Planet. Sci. J.* **2**, 5 (2021).
45. Ingersoll, A. P., Summers, M. E. & Schlipf, S. G. Supersonic meteorology of Io: Sublimation-driven flow of SO $_2$. *Icarus* **64**, 375–390 (1985).
46. Xianzhe, J., Walker, R. J., Kivelson, M. G., Khurana, K. K. & Linker, J. A. Properties of Ganymede's magnetosphere inferred from improved three-dimensional MHD simulations. *J. Geophys. Res. Space Phys.* **114**, A09209 (2009).
47. Duling, S., Saur, J. & Wicht, J. Consistent boundary conditions at nonconducting surfaces of planetary bodies: applications in a new Ganymede MHD model. *J. Geophys. Res. Space Phys.* **119**, 4412–4440 (2014).
48. Fatemi, S., Poppe, A. R., Khurana, K. K., Holmström, M. & Delory, G. T. On the formation of Ganymede's surface brightness asymmetries: kinetic simulations of Ganymede's magnetosphere. *Geophys. Res. Lett.* **43**, 4745–4754 (2016).
49. Plainaki, C. et al. Preliminary estimation of the detection possibilities of Ganymede's water vapor environment with MAJIS. *Planet. Space Sci.* **191**, 105004 (2020).
50. Wirström, E. S., Bjerkeli, P., Rezac, L., Brinch, C. & Hartogh, P. Effect of the 3D distribution on water observations made with the SWI. I. Ganymede. *Astron. Astrophys.* **637**, A90 (2020).
51. Becker, T. M. et al. The far-UV albedo of Europa from HST observations. *J. Geophys. Res. Planets* **123**, 1327–1342 (2018).
52. Roth, L. et al. Constraints on an exosphere at Ceres from Hubble Space Telescope observations. *Geophys. Res. Lett.* **43**, 2465–2472 (2016).
53. Morton, D. C. Atomic data for resonance absorption lines. III. Wavelengths longward of the Lyman limit for the elements hydrogen to gallium. *Astrophys. J. Suppl.* **149**, 205–238 (2003).
54. Gladstone, G. R. Solar O i 1304-Å triplet line profiles. *J. Geophys. Res.* **97**, 19519–19525 (1992).
55. Chandrasekhar, S. *Radiative Transfer* (Dover, 1960).

56. Roth, L., Saur, J., Retherford, K. D., Feldman, P. D. & Strobel, D. F. A phenomenological model of Io's UV aurora based on HST/STIS observations. *Icarus* **228**, 386–406 (2014).
57. McClintock, W. E., Rottman, G. J. & Woods, T. N. Solar-Stellar Irradiance Comparison Experiment II (SOLSTICE II): instrument concept and design. *Sol. Phys.* **230**, 225–258 (2005).
58. Kivelson, M. G. et al. in *Jupiter: The Planet, Satellites and Magnetosphere* (eds Bagenal, F. et al.) 513–536 (Cambridge Univ. Press, 2004).
59. Roth, L. et al. Constraints on Io's interior from auroral spot oscillations. *J. Geophys. Res. Space Phys.* **122**, 1903–1927 (2017).
60. *Ganymede Voyager—Galileo SSI Global Mosaic 1km v1* (United States Geological Survey, 2020); https://astrogeology.usgs.gov/search/map/Ganymede/Voyager-Galileo/Ganymede_Voyager_GalileoSSI_global_mosaic_1km
61. Kanik, I., Johnson, P. V., Das, M. B., Khakoo, M. A. & Tayal, S. S. Electron-impact studies of atomic oxygen: I. Differential and integral cross sections; experiment and theory. *J. Phys. B* **34**, 2647–2665 (2001).

Acknowledgements

L.R. appreciates the support from the Swedish National Space Agency (SNSA) through grant number 154/17 and the Swedish Research Council (VR) through grant number 2017-04897. J.S. acknowledges funding from the European Research Council (ERC) under the European Union's Horizon 2020 research and innovation programme (grant agreement number 884711).

Author contributions

L.R. led the study, performed the data analysis and wrote the manuscript. N.I. supported all steps of the data analysis. G.R.G. contributed to the analysis and interpretation of the COS eclipse test. L.R., J.S., D.G. and B.B. planned and performed the 2010 and 2017 HST observations and observing strategy. All authors contributed to the interpretation of results and manuscript writing.

Competing interests

The authors declare no competing interests.

Additional information

Extended data is available for this paper at https://doi.org/10.1038/s41550-021-01426-9.

Supplementary information The online version contains supplementary material available at https://doi.org/10.1038/s41550-021-01426-9.

Correspondence and requests for materials should be addressed to L.R.

Peer review information *Nature Astronomy* thanks Apurva Oza and Audrey Vorburger for their contribution to the peer review of this work.

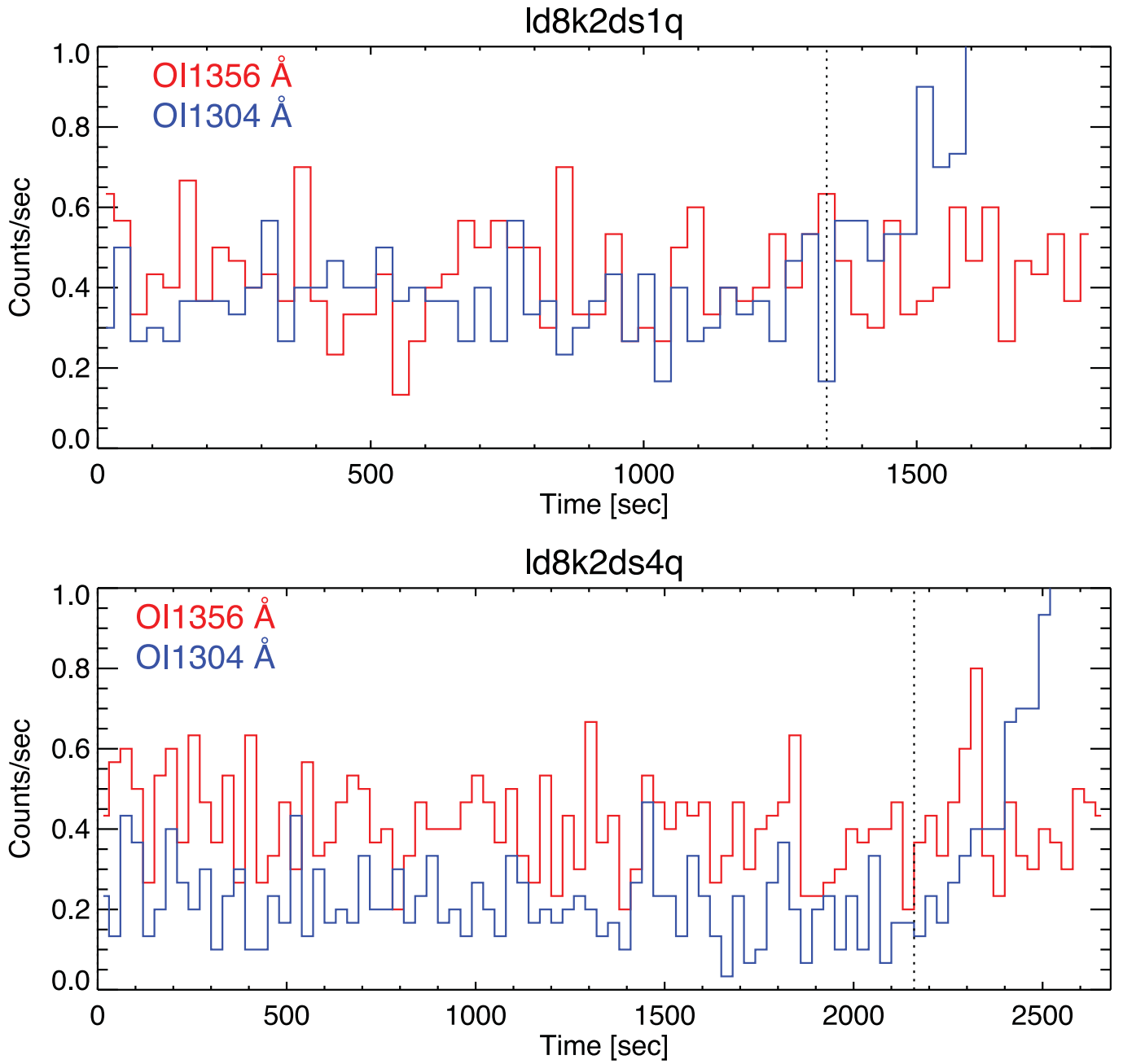

Extended Data Fig. 1 | Count rates at the two oxygen multiplets as a function of time in the COS exposures. A sharp increase of the OI1304 Å emission (blue) from light scattered in the geocorona can be seen towards the end. No increase due to geocoronal scattered light is present at OI1356 Å (red). For the analysis the last 520 s in each exposure are removed in the processing and only the counts left of the vertical dotted lines are used.

Species	Electrons	O_2			O			H_2O			Total		Image-averaged		Image-av.
Scale height	–	H_{O_2} = 100 km			H_O = 400 km			H_{H_2O} = 50 km			model		STIS intensity		ratio
	n_e	n_0	I_{1356}	I_{1304}	n_0	I_{1356}	I_{1304}	n_0	I_{1356}	I_{1304}	I_{1356}	I_{1304}	I_{1356}	I_{1304}	$r_\gamma(OI)$
	[cm^{-3}]	[cm^{-3}]	[R]	[R]	[cm^{-3}]	[R]	[R]	[cm^{-3}]	[R]	[R]	[R]	[R]	[R]	[R]	
Trailing	20	2.8e7	41.3	17.1	5e4	<0.1	2.4	1.2e9*	1.0	5.0	42.3	24.5	42.8±2.0	23.5±1.9	1.8±0.2
Leading	30	2.8e7	58.1	24.1	5e4	<0.1	2.6	2.0e8*	0.4	1.8	58.5	28.5	59.0±1.7	30.2±1.4	2.0±0.1

* maximum at the disk center / at sub-solar point.

Extended Data Fig. 2 | Model atmosphere parameters and results for the corresponding oxygen intensities. The temperature of the electrons is assumed to be T_e = 100 eV. Maps of the model atmospheres are shown in Extended Data Figure 3. Note that the O2 atmosphere produces the vast majority of the OI1356 Å emissions. For the OI1304 Å emissions, in contrast, O_2, O and H_2O all have relevant contributions to the signal.

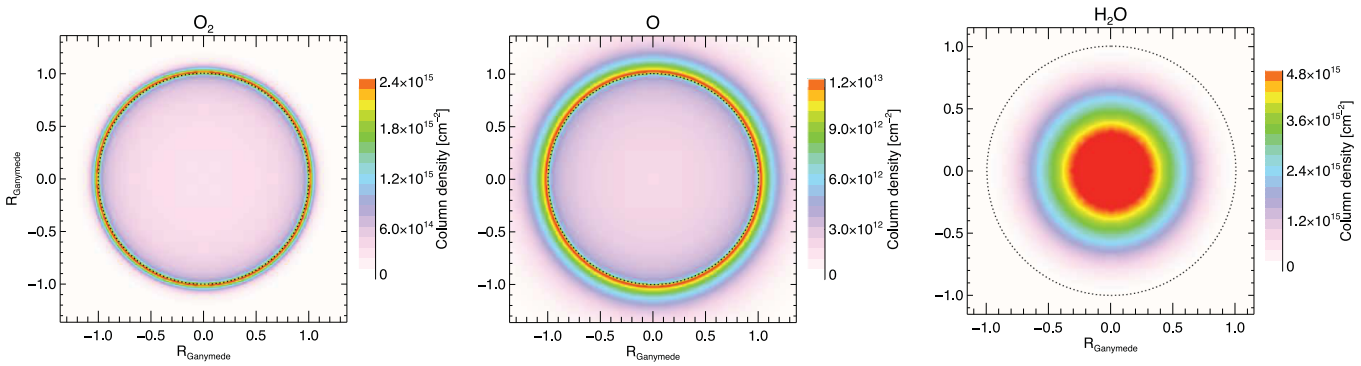

Extended Data Fig. 3 | Column density maps of the model O_2, O and H_2O atmospheres. The H_2O atmosphere is scaled for the best-fit on the trailing hemisphere. The O_2 and O atmosphere are assumed to be identical on the trailing and leading hemispheres. The derived H_2O density for the leading hemisphere is lower by a factor of 6.